Nanoscale and Microscale Thermophysical Engineering, 11: 273–300, 2007

ISSN: 1556-7265 print / 1556-7273 online
DOI: 10.1080/15567260701715370

Taylor & Francis
Taylor & Francis Group

UNIFORM MEMS CHIP TEMPERATURES IN THE NUCLEATE BOILING HEAT TRANSFER REGION BY SELECTING SUITABLE, MEDIUM BOILING NUMBER RANGE

J.L. Xu
Micro Energy System Laboratory, Guangzhou Institute of Energy Conversion, Chinese Academy of Science, Wushan, Guangzhou, P.R. China

Y.H. Gan
School of Electric Power, South China University of Technology, Guangzhou, China

The not only lower but also uniform MEMS chip temperatures can be reached by selecting suitable boiling number range that ensures the nucleate boiling heat transfer. In this article, boiling heat transfer experiments in 10 silicon triangular microchannels with the hydraulic diameter of 155.4 μm were performed using acetone as the working fluid, having the inlet liquid temperatures of 24–40° C, mass fluxes of 96–360 kg/m^{2}s, heat fluxes of 140–420 kW/m^2, and exit vapor mass qualities of 0.28–0.70. The above data range correspond to the boiling number from 1.574×10^{-3} to 3.219×10^{-3} and ensure the perfect nucleate boiling heat transfer region, providing a very uniform chip temperature distribution in both streamline and transverse directions. The boiling heat transfer coefficients determined by the infrared radiator image system were found to be dependent on the heat fluxes only, not dependent on the mass fluxes and the vapor mass qualities covering the above data range. The high-speed flow visualization shows that the periodic flow patterns take place inside the microchannel in the time scale of milliseconds, consisting of liquid refilling stage, bubble nucleation, growth and coalescence stage, and transient liquid film evaporation stage in a full cycle. The paired or triplet bubble nucleation sites can occur in the microchannel corners anywhere along the flow direction, accounting for the nucleate boiling heat transfer mode. The periodic boiling process is similar to a series of bubble nucleation, growth, and departure followed by the liquid refilling in a single cavity for the pool boiling situation. The chip temperature difference across the whole two-phase area is found to be small in a couple of degrees, providing a better thermal management scheme for the high heat flux electronic components. Chen's [1] widely accepted correlation for macrochannels and Bao et al.'s [2] correlation obtained in a copper capillary tube with the inside diameter of 1.95 mm using R11 and HCFC123 as working fluids can predict the present experimental data with accepted accuracy. Other correlations fail to predict the correct heat transfer coefficient trends. New heat transfer correlations are also recommended.

KEY WORDS: microchannels, nucleate boiling heat transfer, uniform chip temperature, flow pattern

This article was supported by the National Natural Science Foundation of China (50776089), the Natural Science Foundation of Guangdong Province (7000742), and the National Key Laboratory on Bubble Physics and Natural Circulation of Nuclear Power Institute.

Address correspondence to J. L. Xu, Micro Energy System Laboratory, Guangzhou Institute of Energy Conversion, Chinese Academy of Science, Nengyuan Road, Wushan Guangzhou, 510640, People's Republic of China. E-mail: xujl@ms.giec.ac.cn

NOMENCLATURE

A_c	cross-sectional area of each triangular microchannel, m^2
b	side wall width of the triangular microchannel, m
$Bo = q/Gh_{fg}$	boiling number
C	Martinelli-Chisholm constant
Co	convection number
c_{pf}	specific heat, J/kgK
d_h	hydraulic diameter of the microchannel, m
E	coefficient in empirical correlations
F	coefficient in empirical correlations
Fr_f	liquid-phase Froude number
G	mass flux, kg/m^2s
h_{exp}	experimental heat transfer coefficient, W/m^2K
h_{fg}	latent heat of evaporation, J/kg
h_{nb}	nucleate boiling heat transfer coefficient, W/m^2K
h_{pred}	predictied of heat transfer coefficient, W/m^2K
h_{sp}	single-phase heat transfer coefficient, W/m^2K
h_{tp}	two-phase heat transfer coefficient, W/m^2K
I	current passing through the thin film heater, A
i	grid in flow direction
i'	grid in flow direction when two-phase area begins
j	grid in the width direction
k_f	thermal conductivity of liquid, W/mK
k_g	thermal conductivity of vapor, W/mK
L_h	total heating length, m
L_{sp}	single-phase liquid flow length, m
M	number of data points
MRE	mean relative error
m	mass flow rate, kg/s
N	total number of parallel microchannels
n_1	exponent in empirical correlations
n_2	exponent in empirical correlations
P_r	reduce pressure
Pr_f	liquid-phase Prandtl number
ΔP	pressure drop for the heat sink with the transverse microchannels, Pa
ΔP_{sat}	change in vapor pressure corresponding to ΔT_{sat}, Pa
Q	effective heating power, W
q	effective heat flux based on the side wall channel area, W/m^2
Re_f	liquid Reynolds number
S	coefficient in empirical correlations
$T_f(z)$	liquid temperature along the flow direction, $^\circ C$
T_{ij}	local chip temperature, $^\circ C$
T_{in}	inlet liquid temperature, $^\circ C$
T_{out}	outlet liquid temperature, $^\circ C$
T_{sat}	saturated temperature, $^\circ C$
$T_w(z,y)$	chip temperature in z and y coordinates, $^\circ C$
$T_{w,ave}$	average chip temperature in the two-phase area, $^\circ C$
ΔT_{sat}	channel wall superheat, $^\circ C$
t	time, s
U	inlet liquid velocity, m/s
V	voltage applied on the thin film, V
We_{fo}	Weber number based on total flow as liquid
X_{tt}	Martinelli parameter based on turbulent liquid-turbulent vapor flow
x	thermodynamic vapor mass quality
x_{out}	exit vapor mass quality
$x(z)$	thermodynamic vapor mass quality along the flow direction
y	width direction coordinate, m
z	flow direction coordinate, m

Greek symbols

η	thermal efficiency
μ_f	liquid viscosity, $Pa \cdot s$
μ_g	vapor viscosity, $Pa \cdot s$
v	kinematic viscosity, m^2/s
ρ_f	liquid density, kg/m^3
ρ_g	vapor density, kg/m^3
σ	surface tension, N/m

Subscripts

exp	experimental
f	liquid phase
g	vapor phase
in	inlet
out	outlet
$pred$	predicted
sat	saturated
sp	single-phase
tp	two-phase
w	chip wall

INTRODUCTION

Since Feynman's thought-provoking speech "There Is a Plenty of Room at the Bottom" in 1959, great progress has been made in the miniaturization of electronic devices. Microelectronics with the integrated circuits and the progress in information industry have changed the way of life, working, discovering, and inventing. Moving to the limit of photolithography, the development pace is expected to slow down to double of the density every 24 months [3].

One of the challenging issues is the cooling technologies that could be used for the high heat flux IC chips. The modern semiconductor devices can have the heat fluxes up to 100 W/cm^2 [4]. The chip should satisfy the temperature limit criterion, such as less than $85°C$. On the other hand, the temperature gradient over the whole chip should be controlled as low as possible. Large temperature gradients induce large thermal stress in the IC components or devices, thus undermining the device reliability. The complex pattern of spatial temperature variations may produce the destructive thermal stress on the interface between the chip and the substrate or heat sink [5]. This is the main reason to seek an isothermal heat sink.

The complementary metal-oxide semiconductor (CMOS) is the main technology for microprocessors and memories. In such microelectronic devices, large temperature variations may cause the imbalances in CMOS devices, affecting the switching speed on temperatures. Workman et al. [6] proposed the physical modeling and studied the temperature effects in the CMOS devices.

In recent years, many articles have dealt with the forced convective single-phase liquid flow and heat transfer in microchannels. This kind of cooling scheme produces a large liquid and chip temperature rise along the flow direction. Meanwhile, the pressure drop across the microchannels should be large due to the small hydraulic diameter of the microchannel used, which requires higher pumping power.

Boiling heat transfer in microchannels is an alternative solution for the high heat flux cooling, in which latent heat is utilized. Low pumping power is required due to the very low flow rate used.

It should be noted that microscale boiling heat transfer is an emerging and new area that attracts both scientists and engineers. It is a quite complicated problem. Selection of the working fluids and operating ranges are essential important for the thermal management of the high heat flux electronic cooling.

Water is not a good working fluid for such applications. Firstly, it has high saturation temperature of $100°C$ at atmospheric pressure. Secondly, it is not suitable to be contact with the active electronics. Because water has a high latent heat of evaporation, boiling in microchannels with water as the working fluid may induce large pressure and temperature oscillations versus time, as reported by Xu et al. [7].

There is an abundance of studies on flow boiling in mini-channels, with the hydraulic diameters ranging from a couple of millimeters to several millimeters. R-113, R-12, R-141b, R-124, R-134a, and Fc-82 are used as the working fluids. Copper, aluminum, and stainless steel capillary tubes or mini-channels were used as the test sections [2,8–17] for the refrigeration application purposes.

At this stage, there are three groups that can be categorized for the boiling heat transfer behaviors in mini-channels. The first group identified the nucleate boiling heat transfer mechanism, with the heat transfer coefficients dependent on the heat fluxes only [4,9,2]. The second group concludes the convective heat transfer

mechanism with the heat transfer coefficients dependent on the mass flux and vapor mass qualities only [4,7]. The third group belongs to the hybrid or some special heat transfer mechanisms [10,11,13,16]. The conflicting conclusions result from different working fluids and operation parameters.

Xu et al. [18] performed microscale boiling heat transfer experiments over a wide range of parameters using acetone as the working fluid. A strong link between the transient flow patterns and the heat transfer coefficients were provided. *The boiling numbers are found to be important for characterizing the heat transfer performances, which can display three distinct regions by dividing the boiling numbers into three subranges*. The heat transfer coefficients can be increased along the flow direction, or the vapor mass qualities at low boiling numbers for $0.69 \times 10^{-3} < Bo < 1.184 \times 10^{-3}$ (region 1). The medium boiling numbers with $1.574 \times 10^{-3} < Bo < 3.219 \times 10^{-3}$ induce the nucleate boiling heat transfer performance, with the constant heat transfer coefficients versus the mass fluxes and vapor mass qualities (region 2). The high boiling numbers for $3.564 \times 10^{-3} < Bo < 5.046 \times 10^{-3}$ result in the decreased heat transfer coefficients versus the vapor mass qualities. The boiling heat transfer coefficients are dependent on the mass fluxes and weak dependent on the heat fluxes (region 3). Both regions 1 and 3 heat transfer modes lead to the uneven chip temperature distributions. Such a study by Xu et al. [18] explains why different conclusions, the nucleate boiling heat transfer mechanism or convective boiling heat transfer mechanism, exist in the public literatures, to some extent.

The nucleate boiling heat transfer mode (region 2) is very useful to maintain a uniform chip temperature distributions. Besides, some disturbances of the pumping flow rate may not influence the temperature level of the chip.

The primary objective of the present article is to propose a better thermal management scheme for the high heat flux IC chip cooling, not only to maintain the low temperature level, but also the low temperature gradients over the whole chip surface, by selecting the suitable boiling number range that ensures the perfect nucleate boiling heat transfer mechanism. Compared with other studies, improvements were made using the silicon chip test section and the infrared radiator image system to deduce the detailed temperature filed measurements across the whole heating area. The heat transfer mechanisms can be identified by the transient flow patterns. The chip surface temperature difference across the whole two-phase area is examined to be small in a couple of degrees. The inlet pressure and inlet/outlet fluid temperatures are found to be stable. The obtained boiling heat transfer coefficients were compared with available corrections for macro- and miniature-scale channels. New correlations were given.

To the authors' knowledge, detailed measurements on the local chip temperatures and heat transfer coefficients for the MEMS evaporator are very scarce.

EXPERIMENTAL SETUP AND PROCEDURE

Silicon Microchannels

The conventional fabricated copper microchannel heat sink has large mass and thermal capacity. Besides, it is difficult to characterize the channel wall surface roughness, which greatly affects the boiling heat transfer behaviors. MEMS evaporator using parallel microchannels are lightweight with small mass and thermal capacity. It

can also be easily integrated with the IC chip and temperature sensors. Thus, it has received much attention in recent years. Based on the typical MEMS fabrication technique, the triangular, rectangular, or trapezoid cross-section microchannel can be used. The base angle for the triangular or trapezoid microchannel is 54.74°. The present MEMS evaporator, as shown in Figure 1, is one of the typical designs using the parallel triangular microchannels. The chip has 10 triangular microchannels with the hydraulic diameter of 155.4 μm, totally covering the width of 4.35 mm and the whole length of 21.45 mm. The whole silicon chip has a length of 30.0 mm and a width of 7.0 mm (the inlet and outlet common plenums are not shown in Figure 1), with the substrate depth of 525 μm. The top of the silicon chip is bonded with a Pyrex glass plate with the thickness of 410 μm, which serves as the insulator and the transparent cover through which the flow patterns can be observed using a high-speed camera system incorporated with a microscope. A thin Pt film was deposited with the effective heating area of 16.0 × 4.2 mm^2, centrally deposited on the back surface of the silicon substrate. A two-dimensional coordinate system was attached on the thin film heater, as shown in Figure 1. The z-coordinate is the streamwise direction and the y-coordinate is perpendicular to the flow direction. An AC power source drives the thin film heater to Simulate the heat source. The silicon microchannels are fabricated using 100 double-polished 4-in. wafers. The microchannels are etched by the wet etching using potassium hydroxide (KOH) and follow the standard MEMS fabrication technique. The power applied on the thin film heater was measured by a powermeter, with an accuracy of 0.5%.

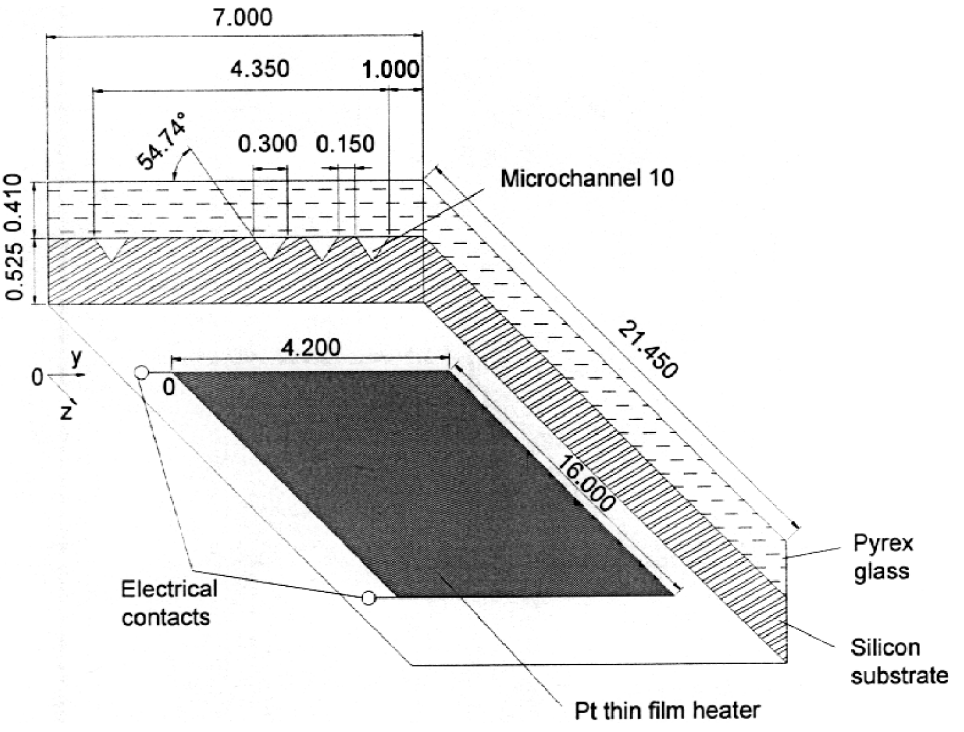

Figure 1. Silicon microchannel test section (all dimensions are in mm).

Experimental Setup

The experimental setup is illustrated in Figure 2, consisting of the liquid supply subsystem, the silicon microchannel test section, and the liquid collection subsystem. The liquid acetone is powered by high-pressure nitrogen gas and flows through a 2-μm precision filter and the silicon microchannel chip. The hot two-phase mixture out of the microchannels is condensed by the cooling water and collected by the glass beaker.

The inlet and outlet fluid temperatures were measured using K-type jacket thermocouples with an accuracy of $0.2°C$. The inlet pressure was measured using a Setra pressure transducer (Model 206, USA), with an accuracy of 1%. The pressure drop across the silicon chip was measured by a Senex differential pressure transducer with the accuracy of 0.1%. The average mass flow rate is determined by the weight increment using a precision electronic balance with the accuracy of 0.02 g, over a given period of time, such as 20 min. The pressure and temperature signals were collected by an HP data acquisition system.

The transient flow patterns were observed by a high-speed camera system bonded with a Leica M stereo-microscope (Wetzlar, Germany). The observed flow length was 6.45 mm relative to the whole microchannel length of 21.45 mm but covering the total width of the 10 triangular microchannels. The observed flow view area was centrally located against the silicon chip. The recording rate of the high-speed camera system was 2000 frames per second.

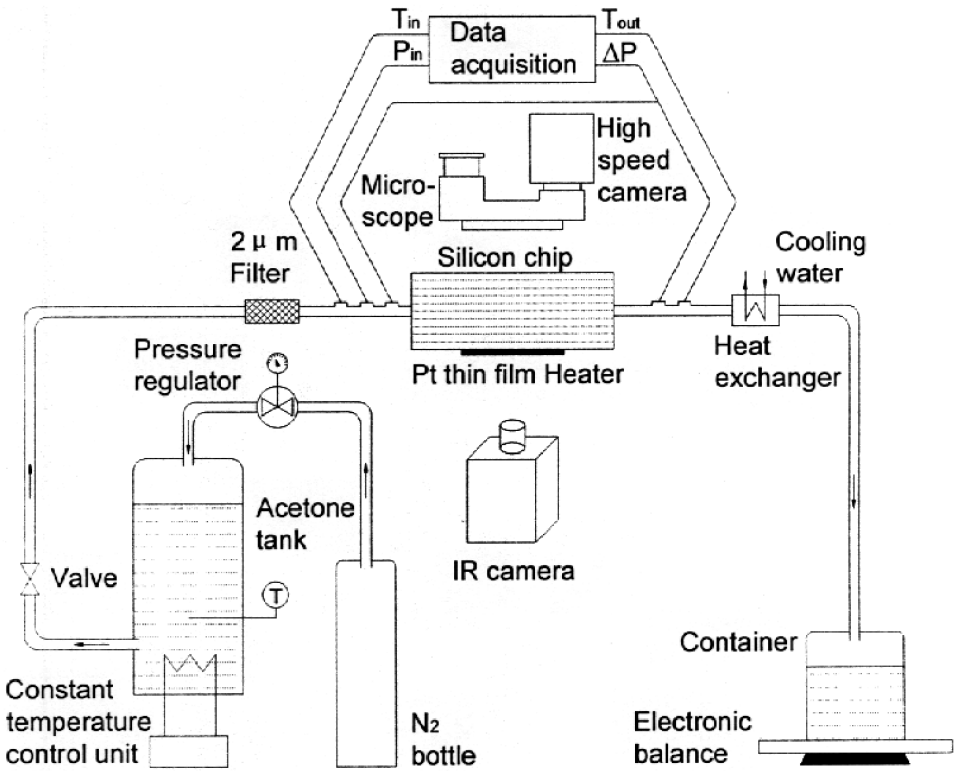

Figure 2. Schematic diagram of the experimental setup.

The surface temperature of the thin-film heater was measured by a high-resolution, high-accuracy infrared radiator image system (FLIR ThermalCAM SC3000IR, USA) with the thermal sensitivity of $0.02°C$ at the temperature of $30°C$, a spatial resolution of 1.1 mrad, and a typical resolution of 320×240 pixels over the focused area. The view area is exactly corresponding to the effective thin-film area of $16.0 \times 4.2\ mm^2$. These parameters assure the precise measurement of the temperature field and the temperature gradients over the selected view area.

Because the IR image measurement of the surface temperatures strongly depends on the emissivity, a thin black lacquer was uniformly deposited on the thin-film heater surface. An emissivity of around 0.94 gives good measurement accuracies of $0.4°C$ after calibration with a set of known standard temperatures. The temperature dependence of emissivity within the considered range can be neglected.

DATA REDUCTION

In the present study the pure acetone liquid is used (CH_3COCH_3, purity $>$ 99.5%, and molecular weight of 58.08). The physical properties are listed in Table 1 at 1 bar saturated condition.

Before the boiling heat transfer experiment, single-phase liquid heat transfer was performed to identify the effective thermal efficiency. The thermal efficiency η is defined as the heat that is received by the liquid (computed from the mass flow rate and the inlet/outlet liquid temperature difference) divided by the applied heating power. The heating power is found to be the major parameter affecting the thermal efficiencies. The larger the heating power is, the higher the thermal efficiency. In the present data range, the measured η has the range from 0.77 to 0.90. Therefore, the average η is set as 0.84. Incorporating such η value induces the uncertainty of 6% for the heat flux. The heat flux is computed as $q = \eta VI/(2NbL_h)$, where V and I are the voltage and current applied on the thin film heater, respectively, N is the total number of microchannels, b is the side wall width, and L_h is the effective heating length.

The liquid Reynolds number is defined as $\mathrm{Re} = Ud_h/v$, where U is the average liquid velocity assuming the total mixture flowing as the liquid only, d_h is the hydraulic diameter of the microchannels, and v is the kinematic viscosity based on the inlet liquid temperature.

The mass flux is calculated as $G = m/(NA_C)$, where m is the mass flow rate determined by the electronic balance and A_C is the cross-sectional area of a single triangular microchannel.

Before performing the heat transfer coefficient analysis, the single-phase liquid flow length should be determined due to the entrance liquid subcooling, which is written as

Table 1 Physical properties of acetone at 1 bar saturated condition

T_{sat} $°C$	ρ_f kgm^{-3}	c_{pf} J/kgK	h_{fg} J/kg	σ N/m	μ_f $Pa \cdot s$	μ_g $Pa \cdot s$	k_f W/mK	k_g W/mK
56.29	748.01	2302.5	512.94	0.0192	2.37×10^{-4}	8.31×10^{-6}	0.518	0.0136

$$L_{sp} = mc_{pf}L_n(T_{sat} - T_{in})/Q \tag{1}$$

where T_m is the inlet liquid temperature and Q is the effective heating power, obtained from the power meter reading timing the thermal efficiency. A linear liquid temperature along the flow direction is assumed along the flow direction in the liquid flow area, which is expressed as

$$T_f(z) = T_{in} + z(T_{sat} - T_{in})/L_{sp} \tag{2}$$

The vapor mass qualities are written as

$$x(z) = \frac{c_{pf}(T_m - T_{sat}) + zQ/mL_h}{h_{fg}} \tag{3}$$

The local heat transfer coefficients are

$$h(z, y) = \frac{q}{T_w(z, y) - T_f(z)} \tag{4}$$

In the single-phase liquid flow area, $T_f(z)$ is calculated using Eq. (2) and x is negative. In the two-phase flow area, $T_f(z)$ uses the saturation temperature and x is positive.

Because the inlet liquid subcooling is small, L_{sp} sometimes covers a couple of millimeters, the maximum L_{sp} is around 4 mm relative to the whole heating length of 16.0 mm. We only focus on the average chip temperature in the two-phase area, which is calculated as

$$T_{w,ave} = \frac{\sum_{j=i}^{152}\sum_{j=l}^{40} T_{ij}}{(152 - i) \times 40} \tag{5}$$

where T_{ij} is the local chip temperature measured by the IR image system. The focused heating area involves totally 6080 data points, i is the longitudinal grid, and j is the transverse grid. Because the single-phase liquid flow area is not included in the average chip temperature calculations, Eq. (5) is integrated starting from the beginning of the two-phase area and i identifies such boundary.

The present experiment yields the following data range: inlet liquid temperatures of 24–40°C, mass fluxes of 96–360 kg/m^2s, heat fluxes of 140–420 kW/m^2, pressure drops of 30–70 kPa, and exit vapor mass qualities of 0.28–0.70. The above date range corresponds to the boiling numbers in the range of 1.574×10^{-3} to 3.219×10^{-3}, ensuring the perfect nucleate boiling heat transfer range. It is noted that the boiling numbers strongly affect the boiling heat transfer mechanisms. Beyond the above boiling number range may result in the increased heat transfer coefficients versus local vapor mass qualities or the convective boiling heat transfer mechanism with decreased heat transfer coefficient versus vapor mass qualities as pointed out in Xu et al. [18].

Table 2 lists all the runs performed in the present study. In order to perform the comparisons between the uniform and nonuniform chip temperature runs, run 0 (the

Table 2 The present microscale boiling heat transfer test runs

Run	q kWm^{-2}	Δp kPa	T_{in} °C	T_{out} °C	G kgm^{-2}s^{-1}	x_{out}	$Bo \times 10^3$	Re	Run	q kWm^{-2}	Δp kPa	T_{in} °C	T_{out} °C	G kgm^{-2} s^{-1}	x_{out}	$Bo \times 10^3$	Re
0	215.3	40.183	31.0	57.5	359.5	0.1700	1.184	191.2	19	288.6	59.609	35.9	57.6	212.9	0.5722	2.699	118.0
1	141.9	30.407	31.3	56.9	110.1	0.5268	2.540	65.2	20	288.6	49.891	38.5	58.3	218.9	0.5685	2.615	124.0
2	149.1	30.212	24.5	57.6	96.1	0.6332	3.058	48.2	21	312.7	51.573	36.6	57.8	205.8	0.6636	3.016	114.8
3	191.2	40.240	34.1	56.9	236.1	0.2919	1.601	128.9	22	324.7	50.092	36.9	57.9	210.5	0.6770	3.061	117.7
4	210.5	60.096	35.3	58.0	253.4	0.2997	1.654	139.8	23	338.0	49.792	37.0	58.8	210.5	0.7110	3.185	117.8
5	214.1	39.956	33.4	59.0	219.6	0.3750	1.928	119.2	24	350.0	50.060	37.2	58.1	223.2	0.6921	3.110	125.1
6	217.7	57.842	35.5	58.4	238.7	0.3406	1.814	131.9	25	358.4	70.242	36.8	57.9	362.0	0.3828	1.978	202.2
7	220.1	39.888	34.4	58.5	200.0	0.4410	2.176	109.5	26	362.0	49.380	37.0	58.6	239.7	0.6615	2.995	134.1
8	224.9	60.213	40.1	57.3	255.1	0.3352	1.755	146.4	27	371.6	49.820	38.1	58.3	249.0	0.6579	2.960	140.6
9	228.5	40.244	32.3	57.2	157.8	0.6088	2.864	84.8	28	371.6	69.766	35.0	59.0	252.1	0.6275	2.947	138.7
10	239.3	40.374	30.0	57.1	155.1	0.6496	3.051	81.8	29	371.6	72.170	35.0	58.4	299.0	0.5100	2.482	164.5
11	239.3	50.133	36.1	57.5	301.7	0.2891	1.574	167.5	30	383.7	70.074	34.7	58.8	247.8	0.6649	3.093	136.0
12	255.0	50.116	39.4	59.1	265.4	0.3898	1.906	151.5	31	383.7	50.600	38.1	58.4	247.5	0.6870	3.075	139.8
13	263.4	59.694	37.1	59.8	253.4	0.4163	2.069	141.9	32	386.1	70.055	35.8	58.8	253.4	0.6567	3.043	140.4
14	264.6	49.911	39.1	59.2	226.0	0.4963	2.322	128.7	33	395.7	70.409	37.4	57.7	277.7	0.6117	2.846	155.9
15	265.8	40.422	32.0	58.1	184.1	0.6109	2.854	98.7	34	396.9	69.522	34.5	58.6	246.2	0.6974	3.219	134.9
16	275.4	40.639	31.8	56.4	180.1	0.6513	3.024	96.4	35	407.7	70.022	37.0	58.4	272.9	0.6466	2.984	152.7
17	276.6	49.985	38.8	59.2	193.7	0.6276	2.834	110.0	36	423.3	60.112	35.6	58.1	289.6	0.6270	2.910	160.1
18	276.6	60.429	36.0	58.7	252.2	0.4408	2.184	139.9	37	360.8	40.949	34.5	58.8	158.8	1.0447	4.492	87.0

Note: Run 0 is for the decreased chip temperatures along the flow direction in the two-phase area, while run 37 is for the increased chip temperatures along the flow direction in the two-phase area.

first run) and run 37 (the last run) are provided for the uneven chip temperatures, induced by the low (region 1 heat transfer mode) and high boiling numbers (region 3 heat transfer mode). Runs 1 through 36 are all for the uniform chip temperature runs at medium boiling number range.

RESULTS AND DISCUSSION

High-Speed Flow Visualization and Microscale Boiling Heat Transfer Mechanism

The IR image system ensures an indirect optical measurement technique for the silicon chip, which does not disturb the temperature field. Boiling heat transfer in microchannels does not always provide a uniform chip temperatures. This is indeed true because different heat transfer mechanisms result in different heat transfer coefficient distributions versus the local vapor mass qualities, or along the flow direction, even though the saturated temperature of the working fluid did not change significantly along the flow direction.

In order to compare the effect of the boiling numbers on the chip temperature distributions, Figure 3 illustrates such distributions for three typical runs measured by the IR image system. As shown in Figure 3, the entrance region of the silicon chip has a relative steep increase for run 0 and run 3 in the single-phase liquid flow area. The steep increased temperatures in the liquid flow area can be further eliminated if one uses the inlet saturated liquid or lower saturation temperature of working fluids. However, distinct distributions appear for the three subfigures followed by the single-phase liquid flow length. Figure 3a shows the decreased (low boiling number performance) and Figure 3c shows the increased chip temperature distributions along the flow direction (high boiling number behavior, displaying the convective boiling heat transfer mechanism). Figure 3b gives the perfect uniform chip temperature distributions beyond the single-phase liquid flow length, corresponding to the medium boiling number.

Transient flow patterns display the *strong periodic behavior in the timescale of milliseconds, including the liquid refilling stage, bubble nucleation, growth and coalesce stage, and transient liquid film evaporation stage*, as shown in Figure 4 for microchannel 8. The white image represents the liquid phase while the black image indicates the vapor phase. The end of the previous cycle or the beginning of a new cycle is shown in Figure 4 at $t = 0$ *ms* when the whole microchannel is full of vapor phase indicated by the black image. Liquid plug flushes the microchannel suddenly at $t = 3.5$ *ms*, separating the whole microchannel as the liquid plug and the vapor slug. During the liquid refilling process, the inverse bubble slugs may be entrained in the long liquid plug, as shown in Figure 4 from $t = 4.5$ *ms* to $t = 8.5$ *ms*.

Bubble nucleation in smooth silicon microchannels with pure working fluid inside has the largest possibilities to take place in the channel corners, which is quite different from that in conventional copper microchannels. With continuous decreasing of the hydraulic diameter of the microchannel, bubble nucleation becomes more difficult and the liquid superheat is increased. Paired or triplet bubbles begin to be nucleated in the corners of the triangular microchannels at the same cross section simultaneously at $t = 9$ *ms*. The quick group bubble growth induces the bubble coalescence at different cross sections along the flow direction at $t = 9.5$ *ms*. The

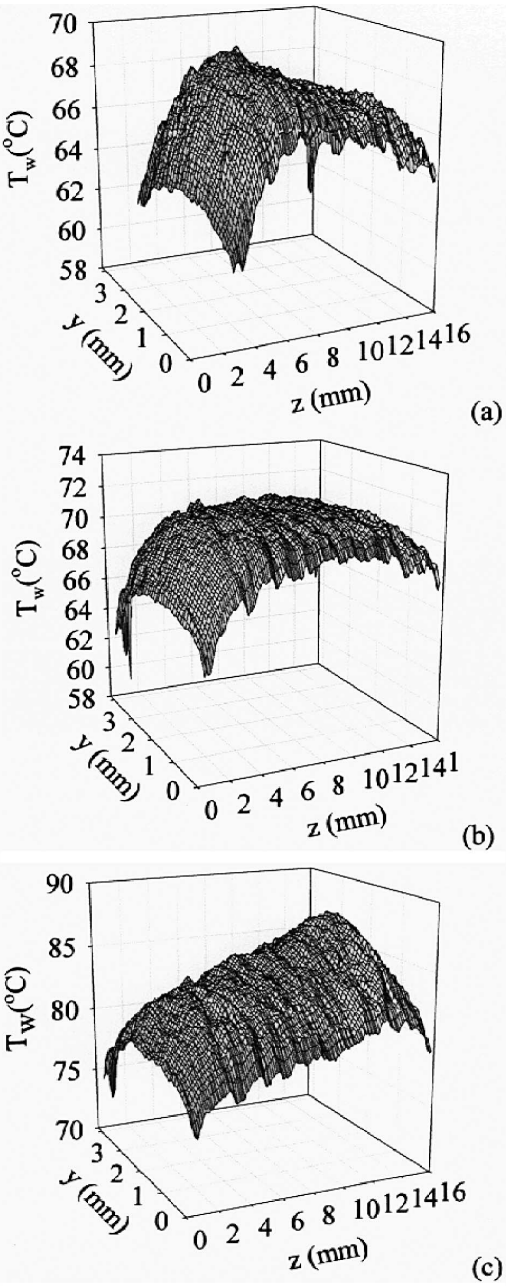

Figure 3. Spatial distributions of chip temperatures. (a) Run 0, $T_{in} = 31.0°C$, $T_{out} = 57.5°C$, $G = 359.5\ kg/m^2s$, $q = 215.3\ kW/m^2$, $Bo = 1.184 \times 10^{-3}$. (b) Run 3, $T_{in} = 34.1°C$, $T_{out} = 56.9°C$, $G = 236.1\ kg/m^2s$, $q = 191.2\ kW/m^2$, $Bo = 1.601 \times 10^{-3}$. (c) Run 37, $T_{in} = 34.5°C$, $T_{out} = 58.8°C$, $G = 158.8\ kg/m^2s$, $q = 360.8\ kW/m^2$, $Bo = 4.492 \times 10^{-3}$.

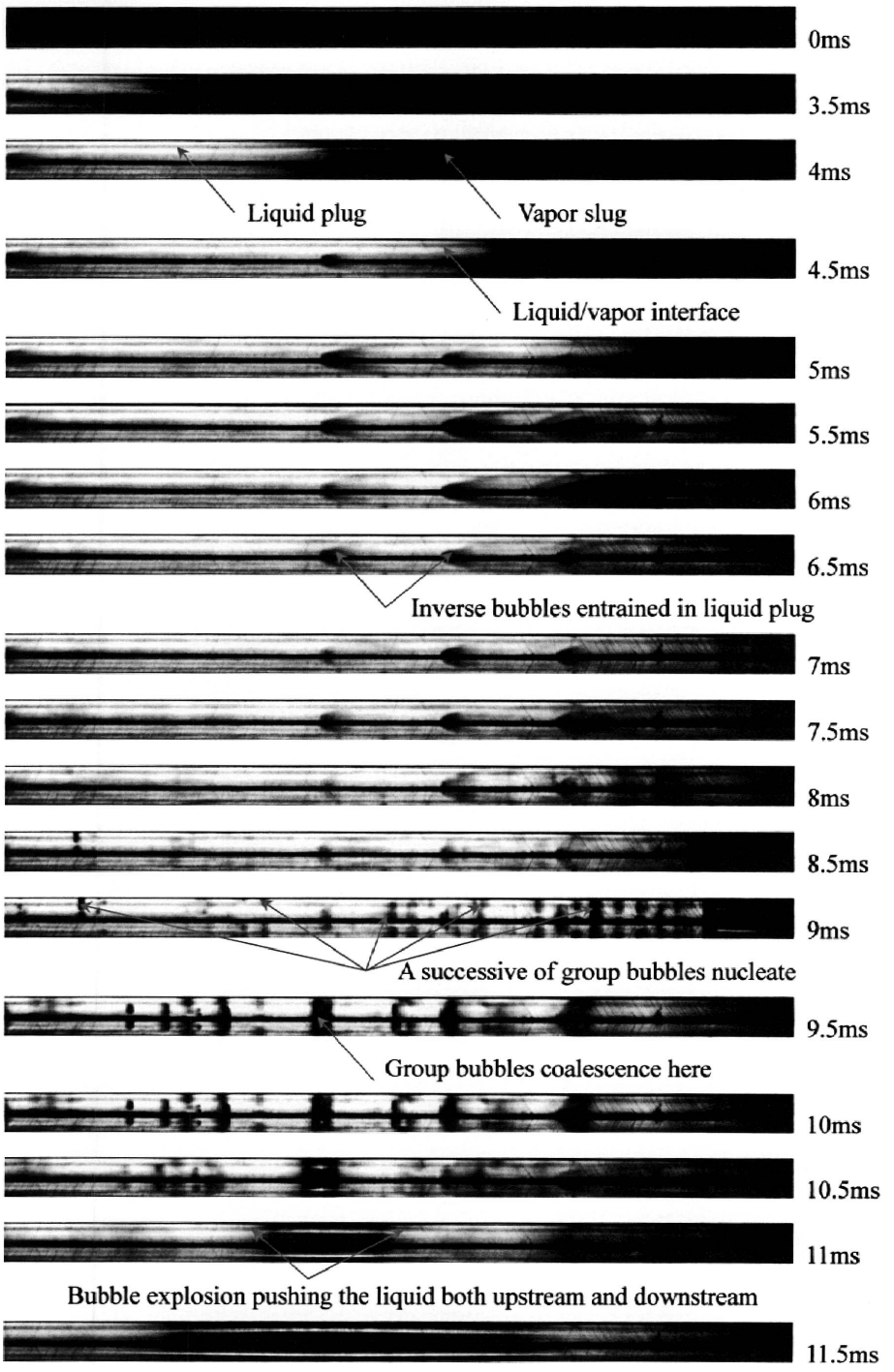

Figure 4. Transient flow patterns in channel 8 for a full cycle (T_{in} = 24.5°C, Δp = 30.21 kPa, G = 96.1 kg/m^{2}s, q = 149.1 kW/m^2, x_{out} = 0.62, Re = 48.2, cycle period = 43.5 ms, $Bo = 3.058 \times 10^{-3}$, run 2).

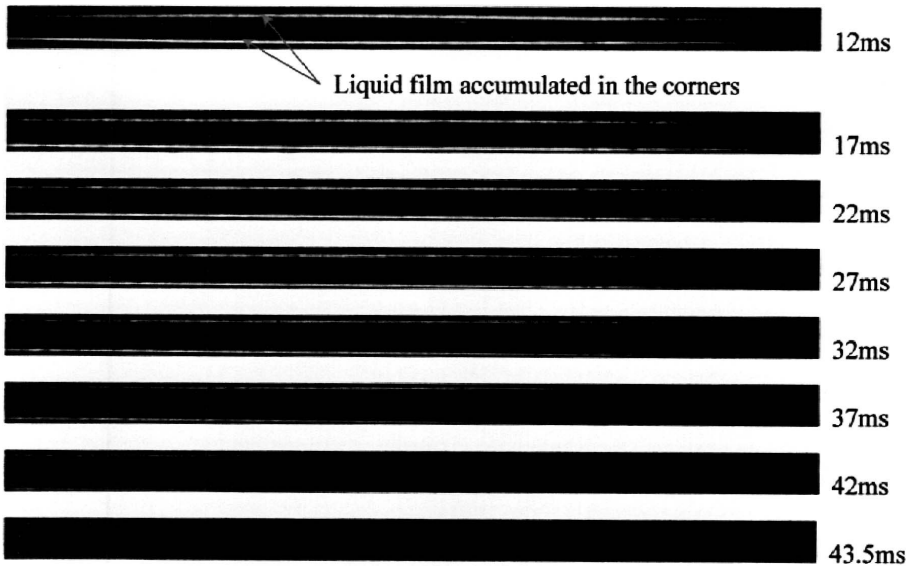

Figure 4. *Continued.*

superheated liquid releases its energy quickly through the coalescence bubble interface, leading to the sharp enlarged bubble slug formed at $t = 11$ *ms*. The bubble explosion further pushes the liquid out of the microchannel at $t = 11.5$ *ms*, leaving the thin liquid films only accumulated in the channel corners, represented by the parallel white lines; see the images from $t = 9$ *ms* to $t = 11.5$ *ms* in Figure 4.

The transient liquid film evaporation stage starts from $t = 11.5$ *ms* and ends at $t = 43.5$ *ms*. In this process, the liquid films accumulated in the corners of the microchannels due to the surface tension force effect, represented by the white lines, become thin versus time, until partial/full dryout occurs and the microchannel returns the state at $t = 0$. A new cycle begins.

The inlet/outlet fluid temperatures, upstream pressure, and pressure drop across the silicon chip are found to be very stable; see Figure 5 for the same run as in Figure 4. This is because the response time of these electronic sensors are much longer than the cycle period of the transient flow patterns. In other words, the pressure and temperature sensors cannot match the fast optical signal variations.

Flow instabilities may take place in boiling two-phase systems in a macro system. The commonly encountered flow instabilities are pressure drop type, density wave type flow instabilities and thermal oscillations. Thermal oscillations may not be independent ones but may accompany the other types of flow instabilities. The available studies such as Hetsroni et al. [5] and Xu et al. [7] show that flow instabilities may also take place in silicon and copper microchannels. These flow instabilities have large oscillation amplitudes of pressure drop, inlet/outlet fluid temperatures, and long cycle periods. At this stage it is not clear what physical mechanisms trigger these flow instabilities. One may suspect that these flow instabilities may be not only related to the heated microchannel itself but also to the whole forced convective loop. The

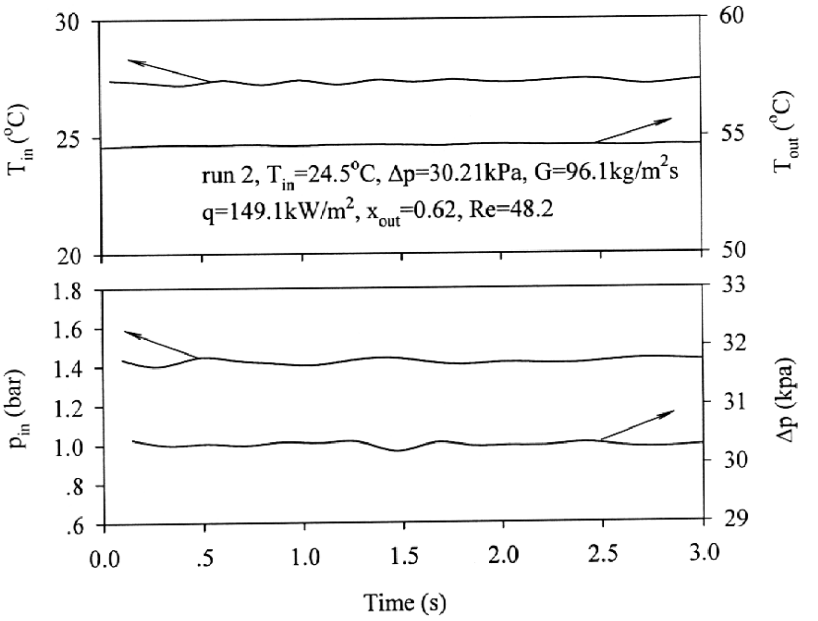

Figure 5. Quasi-stable fluid pressure, pressure drop, and inlet/outlet fluid temperature versus time.

transient flow patterns in the time scale of milliseconds with stable pressure and fluid temperatures are attributed to the physical process inside the silicon chip, not related to the external forced convective loop.

The above transient process in a full cycle involves five heat transfer mechanisms: (1) the single-phase liquid forced convective heat transfer in the liquid refilling stage; (2) the nucleate boiling heat transfer mechanism in the bubble nucleation, growth, and coalescence stage; (3) the vapor explosion – induced forced convective heat transfer mechanism; (4) the transient liquid film evaporation heat transfer mechanism; and (5) the saturated or slight superheated vapor heat transfer mechanism. The detailed description of the transient flow patterns and corresponding heat transfer mechanisms for the low, medium, and high boiling number ranges can be found in Xu et al. [18] and are not repeated here.

It is noted that the vapor explosion – induced liquid traveling velocity is several times than the normal liquid refilling velocity, thus the vapor explosion – induced forced convective heat transfer cannot be neglected, even though the mean liquid Reynolds number is small in microchannels.

The spatial and time statistic characteristic govern which heat transfer mechanism is dominant. It is identified that boiling numbers strongly affect the bubble nucleation site locations. The medium boiling numbers, which are of interest in the present article, lead to the even possibilities of the bubble nucleation sites along the flow direction. Bubble nucleation sites can take place anywhere along the flow direction, from the spatial statistic point of view. *The periodic boiling process is similar to a successive bubble nucleation, growth, and departure followed by the fresh liquid refilling inside a single cavity for a pool boiling situation*. This leads to the nucleate boiling heat transfer mechanism dominant. Both the low and high boiling numbers cause the

uneven bubble nucleation sites along the flow direction, leading to the nonuniform chip temperatures of the silicon chip, which is beyond the scope of the present article.

Further identification of the perfect nucleate boiling heat transfer mode is illustrated in Figure 6 by plotting the centerline heat transfer coefficients versus the streamline vapor mass qualities, in which negative vapor mass qualities indicate the liquid flow area. All six runs shown in Figure 6 illustrate that the boiling heat transfer coefficients are constant versus the local vapor mass qualities. Figure 6a gives the evidence that the boiling heat transfer coefficients are increased with increasing heat fluxes with nearly the same mass flux around of 253 kg/m^2s. Figure 6b shows that the heat transfer coefficients are not influenced by the mass fluxes when the mass fluxes are changed from 184 kg/m^2s to 253 kg/m^2s with the fixed heat flux.

Chip Temperature Distributions at the Nucleating Boiling Heat Transfer Mode

The IR image system clearly identified the chip temperatures focused on the effective heating area of $16.0 \times 4.2\ mm^2$. Figure 7 illustrates such temperatures for the selected 10 runs with the gradual increased heat fluxes. In order to optimize the color

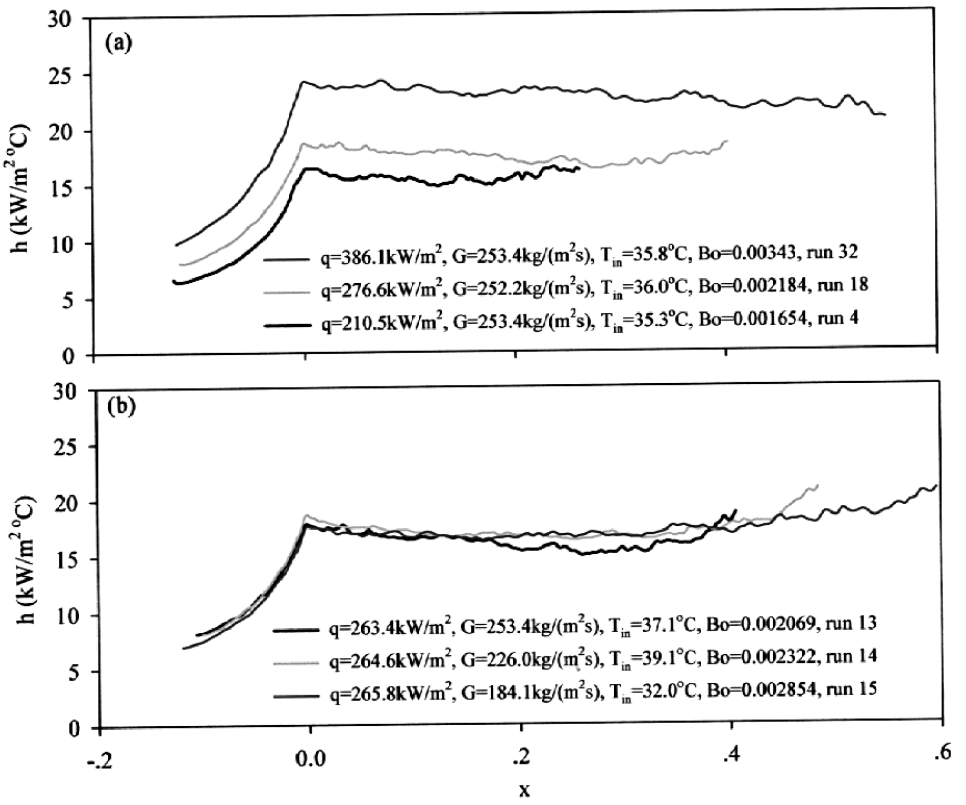

Figure 6. Effects of heat flux q and mass flux G on the heat transfer coefficients for the nucleate boiling heat transfer.

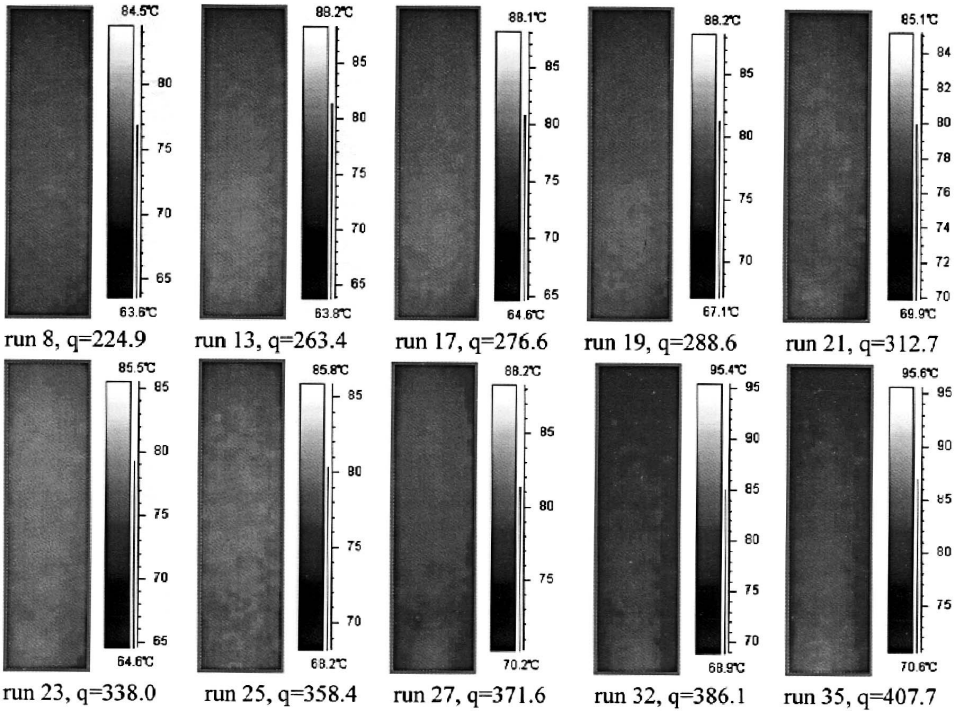

Figure 7. IR image system identified chip temperatures at different heat fluxes.

temperature resolution, different chromatic aberration markings are used for different runs. Indeed, the uniform temperatures can be seen for each run. Generally, higher heat flux causes slight higher chip temperatures.

Figure 8 shows the measured chip temperatures across the width transverse direction at the three axial locations of $z/L_h = 0.25$, 0.50, and 0.75. The parabola chip temperatures are symmetrical distributed against the chip centerline at $y = 2.1$ *mm*. The chip temperature difference across the whole width direction is around $2^{\circ}C$ and is also in a couple of degrees among the three axial locations of $z/L_h = 0.25$, 0.50, and 0.75.

The chip temperatures at the centerline of $y = 2.1$ *mm* are plotted versus the axial coordinates in Figure 9. Along the whole flow direction, the chip temperatures can be categorized into three regions: (1) the single-phase liquid flow area for $z < L_{sp}$, (2) the normal nucleate boiling heat transfer area, and (3) the solid thermal conduction effect area near the ending of the heating length. A slight temperature rise can be identified in the liquid flow area. However, such temperature rise can be further eliminated by using the inlet saturated liquid or using the lower saturation temperature of the working fluids. For the present data range covered, the single-phase liquid flow length covers a couple of millimeters to 4 mm, relative to the whole effective heating length of 16.0 mm. Again, the chip temperatures in the nucleate boiling heat transfer area have no apparent change along the flow direction. The slight temperature decrease close to

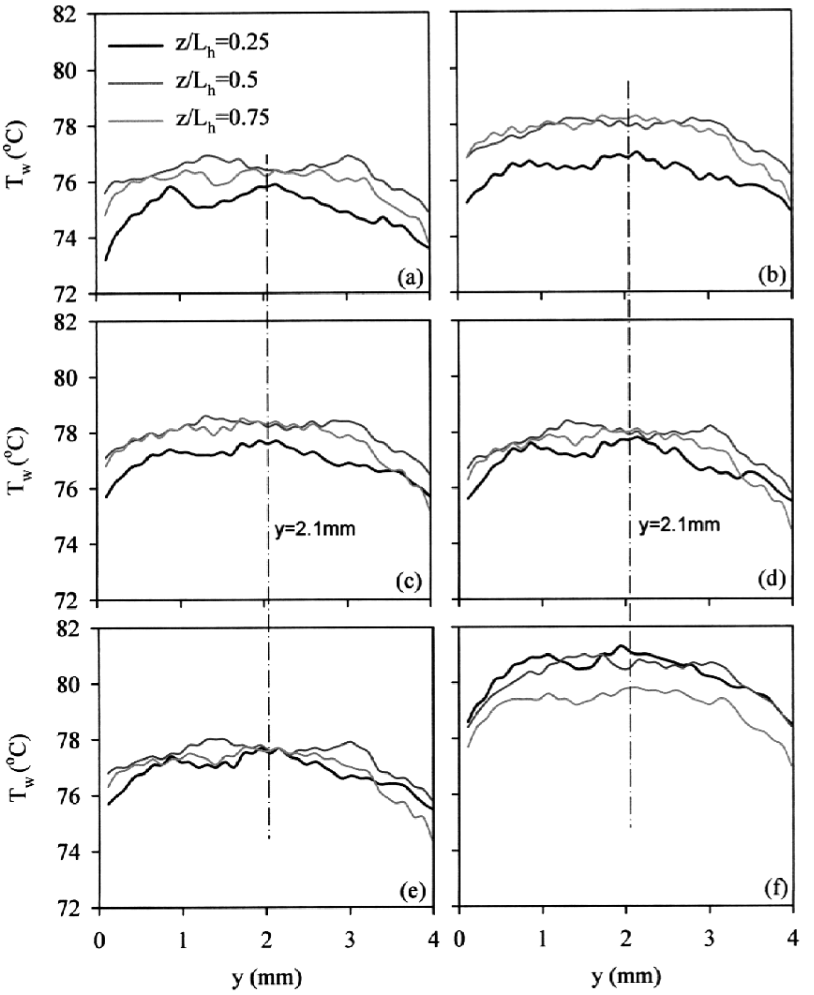

Figure 8. Chip temperature variations in y direction. (a) $q = 224.9$ kW/m^2, $G = 255.1$ kg/m^{2}s, $T_{in} = 40.1$°C, $Bo = 0.001755$, run 8. (b) $q = 265.0$ kW/m^2, $G = 265.4$ kg/m^{2}s, $T_{in} = 39.4$°C, $Bo = 0.001906$, run 12. (c) $q = 264.6$ kW/m^2, $G = 226.0$ kg/m^{2}s, $T_{in} = 39.1$°C, $Bo = 0.002322$, run 14. (d) $q = 276.6$ kW/m^2, $G = 193.7$ kg/m^{2}s, $T_{in} = 38.8$°C, $Bo = 0.002834$, run 17. (e) $q = 288.6$ kW/m^2, $G = 218.9$ kg/m^{2}s, $T_{in} = 38.5$°C, $Bo = 0.002615$, run 20. (f) $q = 371.6$ kW/m^2, $G = 249.0$ kg/m^{2}s, $T_{in} = 38.1$°C, $Bo = 0.002960$, run 27.

the end of the heating area is due to the solid thermal conduction effect across the heated and unheated boundary.

Because both the chip temperatures and boiling heat transfer coefficients are independent of the mass fluxes and vapor mass qualities, the chip temperature superheats, defined as the average chip temperatures in the two-phase area subtracting the saturation temperature of acetone, are plotted in Figure 10 versus the heat fluxes for the total 36 runs. The general trend is the increased temperature superheat with increasing the heat fluxes.

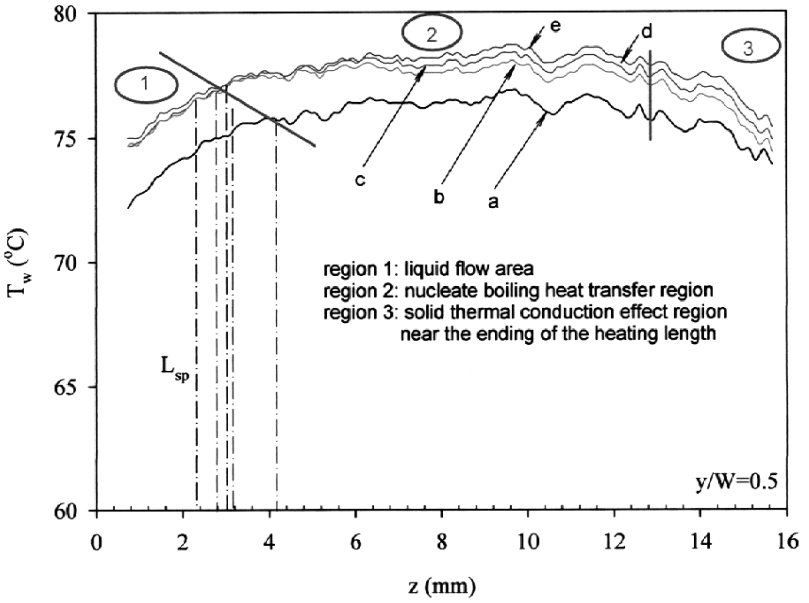

Figure 9. Chip centerline temperature variations along the flow direction. (a) $q = 224.9$ kW/m^2, $G = 255.1$ kg/m^{2}s, $T_{in} = 40.1$°C, $Bo = 0.001755$, run 8. (b) $q = 255.0$ kW/m^2, $G = 265.4$ kg/m^{2}s, $T_{in} = 39.4$°C, $Bo = 0.001906$, run 12. (c) $q = 264.6$ kW/m^2, $G = 226.0$ kg/m^{2}s, $T_{in} = 39.1$°C, $Bo = 0.002322$, run 14. (d) $q = 276.6$ kW/m^2, $G = 193.7$ kg/m^{2}s, $T_{in} = 38.8$°C, $Bo = 0.002834$, run 17. (e) $q = 288.6$ kW/m^2, $G = 218.9$ kg/m^{2}s, $T_{in} = 38.5$°C, $Bo = 0.002615$, run 20.

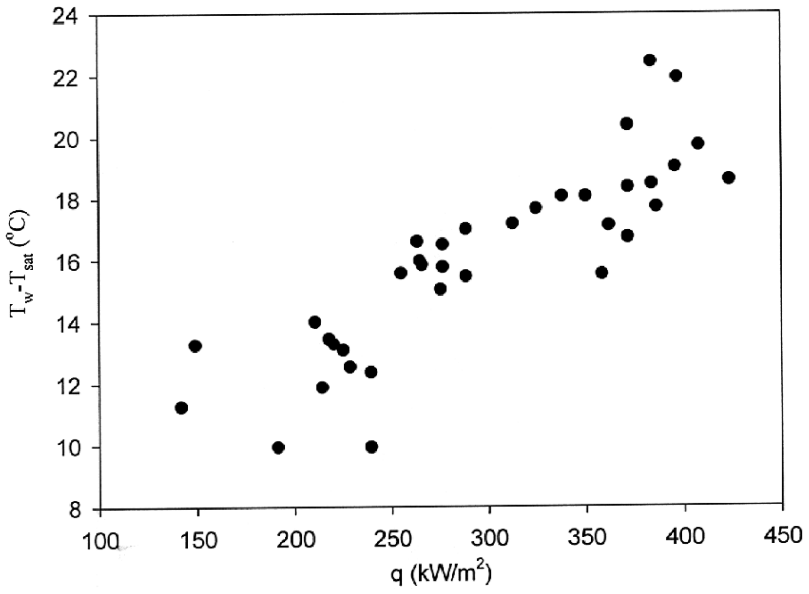

Figure 10. Chip temperature superheat versus heat fluxes for the nucleate boiling heat transfer ($T_{in} = 24.5$–$40.1°C$, $G = 96.1$–362.0 kg/m^{2}s, $\Delta p = 30.21$–72.17 kPa, $Bo = 0.001474$–0.003355).

Comparisons of the Boiling Heat Transfer Coefficients with Available Correlations

Compared with Macrochannel Correlations There are many boiling heat transfer coefficient correlations in macroscale. The well-known Chen's correlation [1] takes account of the two heat transfer mechanisms: the boiling heat transfer contribution plus the forced convective heat transfer contribution. It is noted that the correlation is based on the fully developed turbulent flow in macrochannels. Chen's original correlation is written as

$$h_{ip} = Sh_{nb} + Eh_{sp} \tag{6}$$

where h_{nb} and h_{sp} are the nucleate boiling heat transfer contribution and the forced convective heat transfer contribution, respectively. S is the suppression factor and is related to the two-phase Reynolds number. E is used to adjust the forced convective heat transfer component contributed to the whole heat transfer coefficient and is related to the parameter X_{tt}. Because Chen's correlation has two coefficients to balance the two heat transfer mechanism contributions, it has been widely applied for the heat transfer predictions in various vertical macrotubes with many working fluids. It can also be extended to the subcooled flow boiling heat transfer analysis with acceptable accuracy.

The concept of two heat transfer mechanism contribution is used to develop some other correlations, such as Gungor and Winterton [19], Liu and Winterton [20], Steiner and Taborek [21], etc. These correlations are listed in Table 3 and they are also employed by Bao et al. [2] and Qu and Mudawar [17] to evaluate the boiling heat transfer behaviors in copper capillary tube and microchannel heat sinks. In the present study we use these correlations to evaluate the local boiling heat transfer coefficients. For each correlation, the mean relative error is defined as

$$MRE = \frac{1}{M}\sum \frac{\left|h_{pred} - h_{tp,\exp}\right|}{h_{tp,\exp}} \times 100\% \tag{7}$$

Two random runs are selected for the comparisons between the measured local boiling heat transfer coefficients and the predictions using the available correlations. The results are plotted as $h_{pred}/h_{\exp}$ versus local vapor mass qualities, x, in Figure 11 and the MRE values are listed in Table 3. It is seen that Chen's correlation [1] and Liu and Winterton's correlation [20] give the MRE values of 17.9% and 13.9%, respectively, indicating that the two correlations are still acceptable for the rough heat transfer estimations even for the boiling heat transfer in microchannels.

Other correlations overpredict the boiling heat transfer coefficients. The reasons can be summarized as follows: (1) These correlations are developed based on the database in macrochannels, which have much larger channel diameters. In a two-phase system, extrapolating a correlation to other operating conditions beyond those for which the correlation was originally developed can lead to apparent errors. (2) The present operating conditions, such as working fluid used, heat fluxes, and mass fluxes, are significant different from those that the correlations were originally developed. (3) In macroscale channels, the flow is fully turbulent. However, laminar flow exists in microchannels due to the low Reynolds number. (4) The conventional channels have

Table 3 Flow boiling heat transfer correlations for macrochannels

Author	Correlations for heat transfer coefficient	MRE (%)
Chen [1]	$h_{tp} = Sh_{nb} + Eh_{sp}$ $h_{nb} = 0.00122\frac{k_f^{0.79}c_{pf}^{0.45}\rho_f^{0.49}}{\sigma^{0.5}\mu_f^{0.29}h_{fg}^{0.24}\rho_g^{0.24}}\Delta T_{sat}^{0.24}\Delta p_{sat}^{0.75}, \quad S = 0.9622 - 0.5822\tan^{-1}\left(\frac{\mathrm{Re}_f E^{1.25}}{6.18\times10^4}\right)$ $h_{sp} = 0.023\mathrm{Re}_f^{0.8}\mathrm{Pr}_f^{0.4}\frac{k_f}{d_h}, \quad E = \left(1+\frac{1}{X_{tt}^{0.5}}\right)^{1.78}, \quad \mathrm{Re}_f = \frac{G(1-x)d_h}{\mu_f}$ $\mathrm{Pr}_f = \frac{c_{pf}\mu_f}{k_f}, X_{tt} = \left(\frac{1-x}{x}\right)^{0.9}\left(\frac{\rho_g}{\rho_f}\right)^{0.5}\left(\frac{\mu_f}{\mu_g}\right)^{0.1}$	17.9
Gungor and Winterton [19]	$h_{ip} = Sh_{nb} + Eh_{sp}$ $h_{nb} = 55p_r^{0.12}[-\log_{10}(p_r)]^{-0.55}M^{-0.5}q^{0.67}, \quad S = \left(1+1.15\times10^{-6}E^2\mathrm{Re}_f^{1.17}\right)^{-1}$ $h_{sp} = 0.023\mathrm{Re}_f^{0.8}\mathrm{Pr}_f^{0.4}\frac{k_f}{d_h}, \quad E = 1+24000Bo^{1.16}+1.37\left(\frac{1}{X_{tt}}\right)^{0.86}$ *When* $Fr_f \le 0.05$, *replace E by* $EFr_f^{0.1-2Fr_f}$ *and S by* $SFr_f^{0.5}$	237.0
Liu and Winterton [20]	$h_{tp} = [(Sh_{nb})^2 + (Eh_{sp})^2]^{1/2}, \mathrm{Re}_{fo} = \frac{Gd_h}{\mu_f}$ $h_{nb} = 55p_r^{0.12}[-\log_{10}(p_r)]^{-0.55}M_w^{-0.5}q^{0.67}, \quad S = \left(1+0.055E^{0.1}Re_{fo}^{1.16}\right)^{-1}$ $h_{sp} = 0.023\mathrm{Re}_{fo}^{0.8}\mathrm{Pr}_f^{0.4}\frac{k_f}{d_h}, \quad E = \left[1+x\mathrm{Pr}_f\left(\frac{\rho_f}{\rho_g}-1\right)\right]^{0.35}$ *When* $Fr_l \le 0.05$, *replace E by* $EFr_f^{0.1-2Fr_f}$ *and S by* $SFr_f^{0.5}$	13.9

Steiner and Taborek [21]	$h_{tp} = [(Sh_{nb})^3 + (Eh_{sp})^3]^{1/3}$ $h_{nb} = 3270\,(for\ acetone), \quad S = F\left(\frac{q}{20000}\right)^{0.5-0.1\exp(1.75p_r)}\left(\frac{d_h}{0.01}\right)^{-1.4} f(M)$ $h_{sp} = 0.023\mathrm{Re}_{fo}^{0.8}\mathrm{Pr}_f^{0.4}\frac{k_f}{d_h}, \quad E = \left[(1-x)^{1.5} + 1.9x^{0.6}\left(\frac{\rho_f}{\rho_g}\right)^{0.35}\right]^{1.1}$ $F = 2.816p_r^{0.45} + \left(3.4 + \frac{1.7}{1-p_r^7}\right)p_r^{3.7}$ $f(M) = 0.377 + 0.199\ln\ M_w + 0.000028427\ M_w^2$	335.6
Shah [22,23]	$h_{tp} = \max\ (E,S)h_{sp}, \quad h_{sp} = 0.023\mathrm{Re}_f^{0.8}\mathrm{Pr}_f^{0.4}\frac{k_f}{d_h}, \quad S = 1.8/N^{0.8}$ $When\ N > 1.0, \quad E = 230Bo^{0.5}(Bo > 0.00003) \quad E = 1 + 46Bo^{0.5}(Bo < 0.00003)$ $When\ 0.1 < N \le 1.0, \quad E = FBo^{0.5}\ \exp(2.74N^{-0.1})$ $When\ N \le 0.1, \quad E = FBo^{0.5}\exp(2.74N^{-0.15})$ $N = Co\ (Fr_f \ge 0.04) \quad N = 0.38Fr_f^{-0.3}Co\ (Fr_f < 0.04)$ $F = 14.7\ (Bo \ge 0.0011) \quad F = 15.43\ (Bo < 0.0011)$ $Co = \left(\frac{1-x}{x}\right)^{0.8}\left(\frac{\rho_g}{p_t}\right)^{0.5}, \quad Fr_f\frac{G^2}{\rho_f^2 g d_h}$	84.7
Kandlikar [24]	$h_{tp} = \max(E,S)h_{sp}, \quad h_{sp} = 0.023\mathrm{Re}_f^{0.8}\mathrm{Pr}_f^{0.4}\frac{k_f}{d_h}$ $E = 0.6683Co^{-0.2}f(Fr_f) + 1058Bo^{0.7}$ $S = 1.136Co^{-0.9}f(Fr_f) + 667.2Bo^{0.7}$ $f(Fr_f) = 1\ (Fr_f \ge 0.04)\ or\ f\ (Fr_f) = (25Fr_f)^{0.3}\ (Fr_f < 0.04)$	62.9

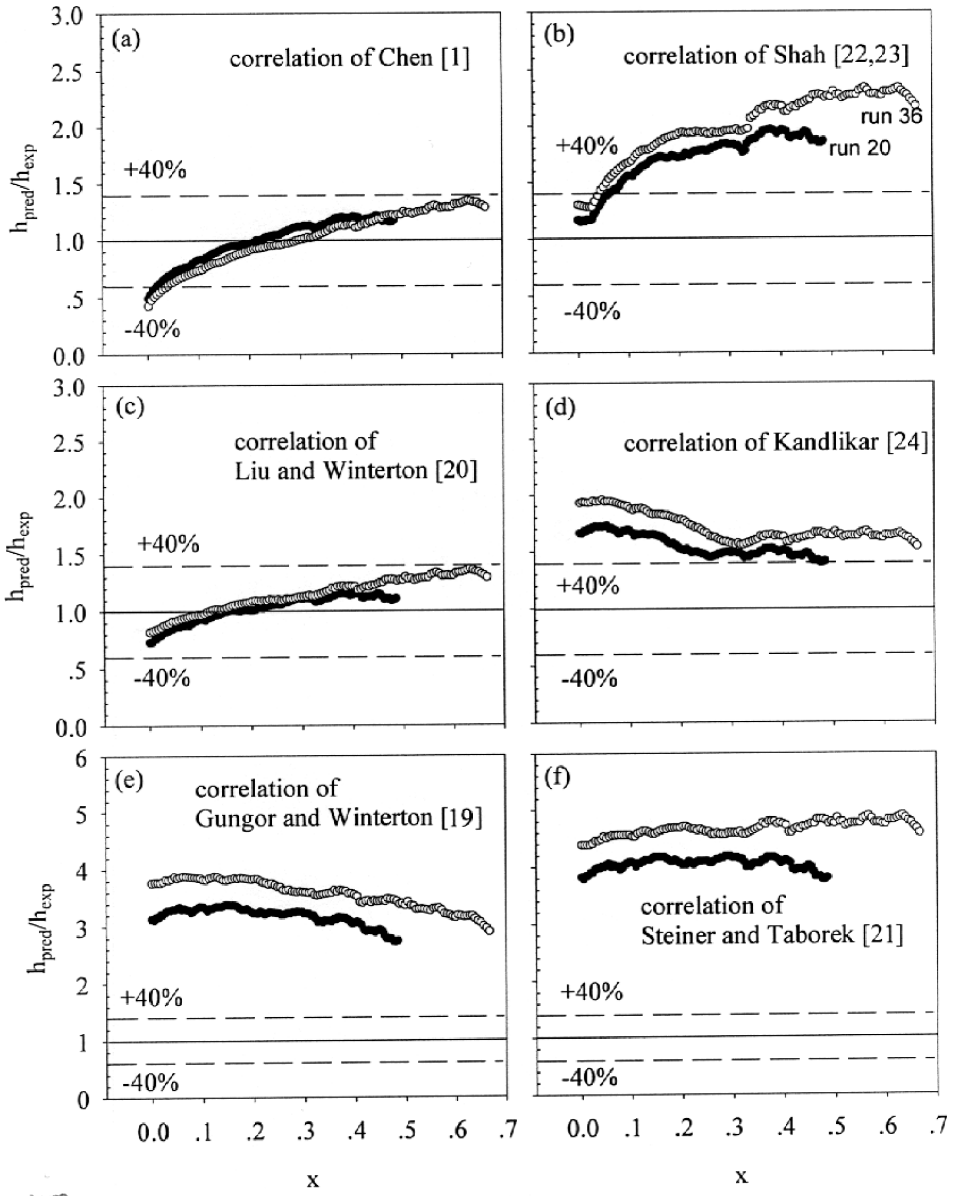

Figure 11. Comparisons of the measured local boiling heat transfer coefficients with macrochannel correlations for two runs: (1) $q = 288.6$ kW/m^2, $G = 218.9$ kg/m^{2}s, $T_{in} = 38.5°$C, $Bo = 0.002615$, run 20; (2) $q = 423.3$ kW/m^2, $G = 289.6$ kg/m^{2}s, $T_{in} = 35.6°$C, $Bo = 0.002910$, run 36.

much rougher wall surface than the silicon wall surface, leading to the enhanced boiling heat transfer in conventional channels.

Compared with Miniature Channel Correlations Some miniature-scale boiling heat transfer experiments have been reported in the literature. Bao et al. [2] investigated the boiling heat transfer in copper capillary tube with an inner diameter of

1.95 mm with Freon R11 and HCFC123 as the working fluids. The heat fluxes ranged from 5 to 200 kW/m^2 and mass fluxes from 50 to 1800 kg/m^2s with the system pressures from 2 to 5 bar. The boiling heat transfer coefficients are found to be strongly dependent on the heat fluxes. The effects of mass fluxes and vapor mass qualities are quite small, displaying the nucleate boiling heat transfer mode.

Two-phase pressure drop, boiling heat transfer, and critical heat flux have been studied by Yu et al. [16] in a 2.98-mm inside diameter tube with the heating length of 0.9 m using water as the working fluid. The mass fluxes ranged from 50 to 200 kg/m^2s. Experimental results and comparisons with the state-of-art predictive correlations were presented. Other miniature-scale boiling heat transfer experiments were performed by Lazarek and Black [8] and Tran et al. [10].

Generally there are two types of boiling heat transfer coefficient correlations available in the literatures. The boiling heat transfer is either directly correlated in the form of $h_{tp} = Cq^n$ or $h_{tp} = C_1(Bo^2We_{fo})^{n_1}(\rho_g/\rho_f)^{n_2}$, where C, C_1, C_2, n_1, n_2 are different for different working fluids and operating conditions. The first type is only suitable for the nucleate boiling heat transfer, such as correlations by Bao et al. [2]. The second type, such as in Tran et al. [10] and Yu et al. [16], relate both the heat fluxes and mass fluxes with the boiling heat transfer coefficients. The above correlations are summarized in Table 4.

Because the present experiment displays the perfect nucleate boiling heat transfer mode, comparisons of the boiling heat transfer coefficients for all 36 runs with the available correlations are shown in Figure 12. It is seen that the correlation by Bao et al. [2] slightly overpredicts our experimental data (MRE of 22.3% and 16.7% for the two working fluids), but the errors for all 36 runs lie in the range of 40%. The correlation by Yu et al. [16] greatly overpredicts the present experimental data (MRE of 438.7%). In contrast to those of Lazarek and Black [8] and Yu et al. [16], Tran et al. [10] greatly underpredict the present experimental data (MRE of 89.3%).

As reported, the correlation by Yu et al. [16] provides the better agreement with Qu and Madawar's [17] experimental data in copper microchannel heat sink consisting of 21 parallel microchannels with the cross section of $231 \times 713\ \mu m$. However, Yu et al.'s [16] correlation fails to correlate the present experimental data in silicon triangular microchannels.

Table 4 Flow boiling heat transfer correlations for mini-channels and microchannels

MRE (%)	Correlations for heat transfer coefficient	Author
61.9	$h_{tp} = 30\mathrm{Re}_{fo}^{0.857}\ Bo^{0.714}\frac{k_f}{d_h}$	Lazarek and Black [8]
89.3	$h_{tp} = 8.4 \times 10^5 (Bo^2We_{fo})^{0.3}\left(\frac{\rho_g}{\rho_f}\right)^{0.4},\ We_{fo} = \frac{G^2 d_h}{\rho_f \sigma}$	Tran et al. [10]
22.3	$h_{tp} = 2.229q^{0.735},\ for\ R11$	Bao et al. [2]
16.7	$h_{tp} = 2.835q^{0.712},\ for\ HCFC123$	
438.7	$h_{tp} = 6.4 \times 10^6 (Bo^2We_{fo})^{0.24}\left(\frac{\rho_g}{\rho_f}\right)^{0.2}$	Yu et al. [16]

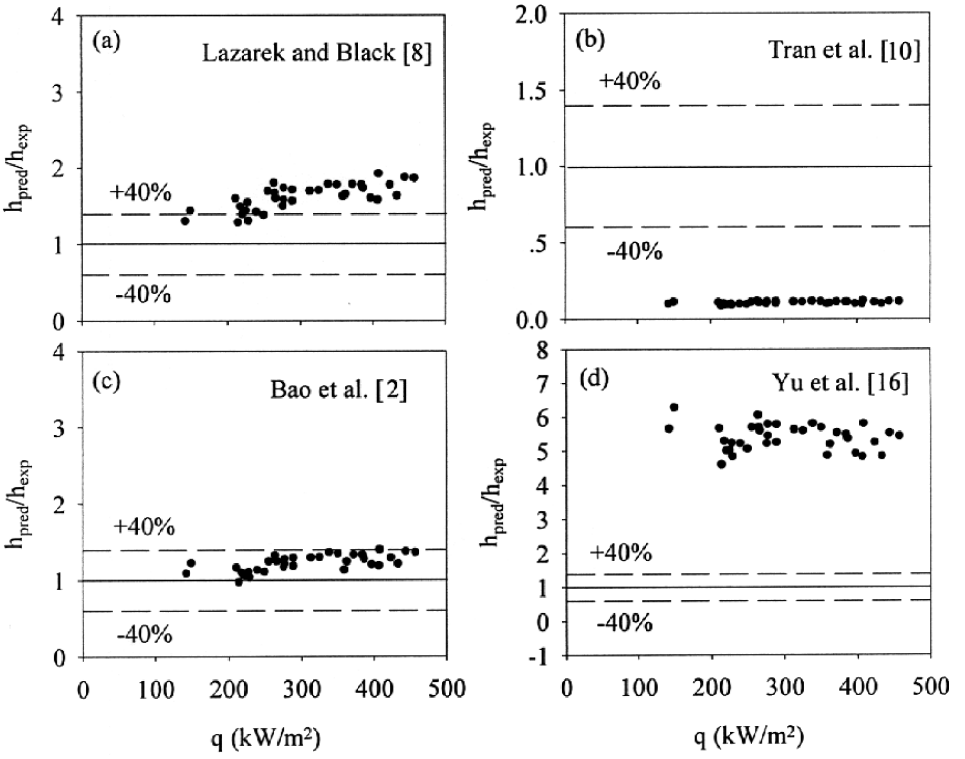

Figure 12. Comparisons of the measured boiling heat transfer coefficients for the 36 runs with miniature channel correlations ($T_{in} = 24.5$–$40.1°C$, $G = 96.1$–362.0 kg/m^{2}s, $\Delta p = 30.21$–72.17 kPa, $Bo = 0.001474$–0.003355).

Short Discussion of the Available Correlations and the New Correlations It should be emphasized that deviations from the experimental trends are not related to the weakness of the correlations themselves but more to the unique nucleate boiling heat transfer in smooth silicon microchannels. Among all the 10 correlations listed in Tables 3 and 4, Bao et al. [2], Chen [1], and Liu and Winterton [20] give the reasonable prediction of the present experimental data trends. The predictive capability of the correct trend of the experimental data by Chen's [1] correlation indicates that such correlation can also be extended down to microscale. It may be accidental that the Bao et al.'s [2] correlation matches the present data trend, even though both show the nucleate boiling heat transfer behaviors. Most other correlations greatly overpredict the present experimental data. The wall surface of the conventional stainless tube, copper microchannel, etc., is much rougher than the silicon wall surface, inducing the higher boiling heat transfer coefficients in the conventional channels.

In the present data range covered, the boiling heat transfer coefficients are correlated as $h_{tp} = 2.5q^{0.709}$, which is similar to that of Bao et al. [2]. Alternatively, the boiling heat transfer coefficients are also correlated as $h_{tp} = 1052830(Bo^2We_{fo})^{0.2573}\ (\rho_g/\rho_f)^{0.1408}$ with an MRE of 5.8%. The comparisons of the present correlations and the experimental data are shown in Figures 13 and 14 for the two correlations, respectively.

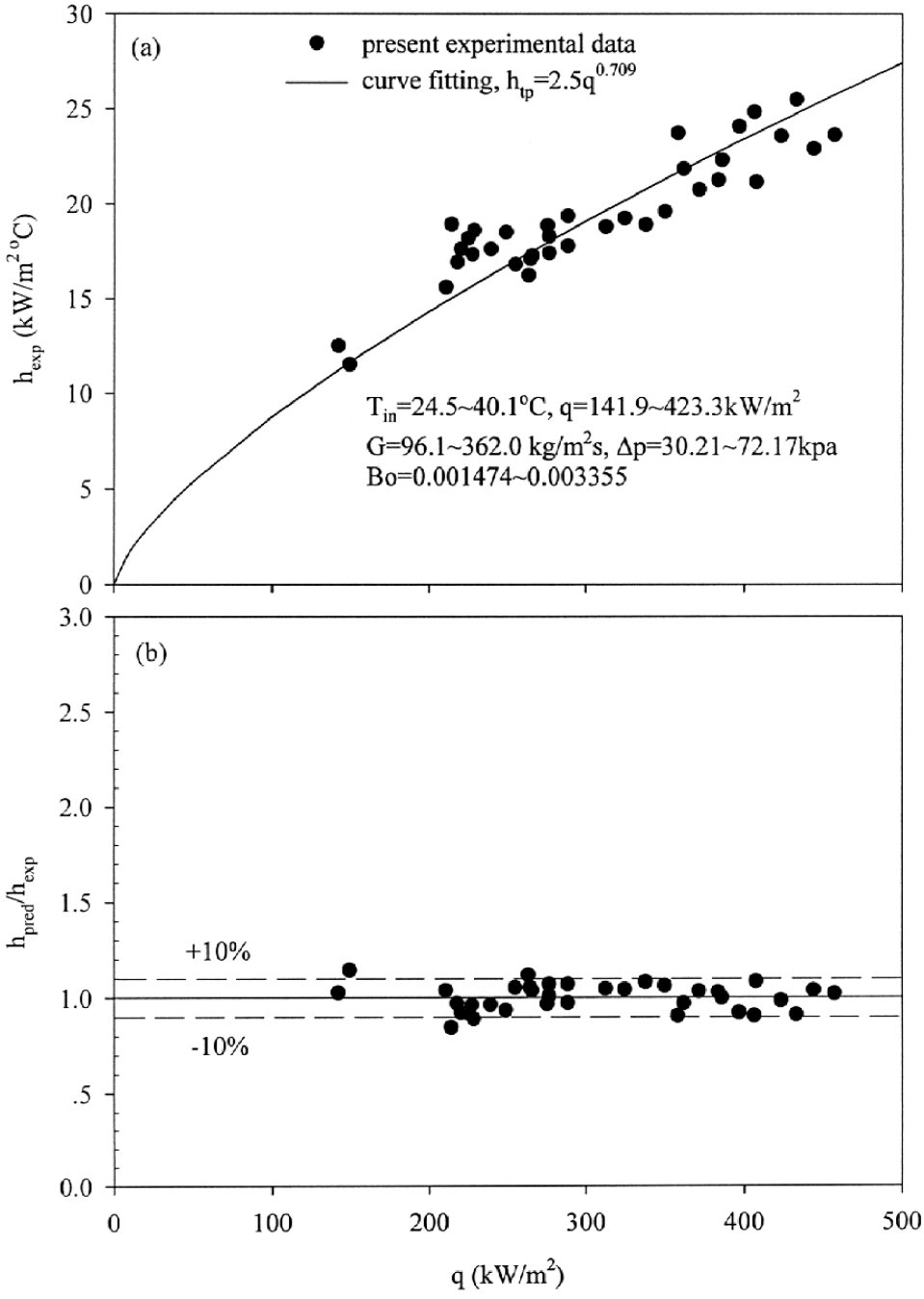

Figure 13. The present boiling heat transfer correlation.

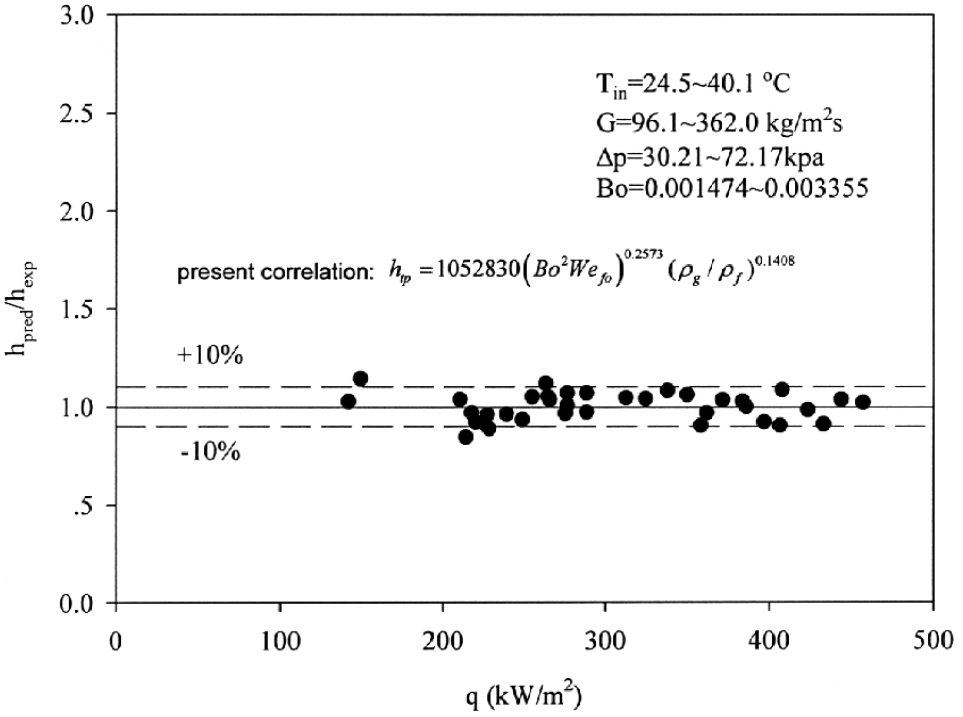

Figure 14. An alternative boiling heat transfer coefficient correlation with the mean relative error of 5.8%.

COMMENTS AND DISCUSSIONS

We propose a better thermal management scheme to maintain not only the low temperature but also the low temperature gradient by selecting the suitable boiling number range that ensures the nucleate boiling heat transfer. Compared with water, which has high saturation temperature, large surface tension force, and latent heat of evaporation, some low saturation temperature working fluids with low surface tension force may have wide operation range in the nucleate boiling heat transfer mode where as microchannel heat sink using water as the working fluid may have wide operation range in annular flow. The nucleate boiling heat transfer induces the heat transfer coefficients and chip temperatures not influenced by mass fluxes and vapor mass qualities, or the streamwise coordinate.

Another advantage of the nucleate boiling heat transfer for the thermal management of the electronic device is that the cooling condition is not influenced by the disturbance of the forced convective loop, such as the flow rate and pumping power, because the heat transfer coefficients are not affected by the mass flow rate, providing that the nucleate boiling heat transfer can be sustained.

The disadvantage of the increased chip temperature in the entrance region due to the inlet liquid subcooling can be eliminated by increasing the inlet liquid temperature or using lower saturation temperature of the working fluids.

CONCLUSIONS

Our experimental studies indicate that microscale boiling heat transfer can display either the convective boiling or nucleate boiling heating transfer mechanisms, depending on the boiling number ranges. Boiling heat transfer in MEMS evaporator is significantly different from that in conventional copper microchannel heat sinks due to the very smooth wall surface. It behaves the strong periodic characteristics with liquid refilling stage, bubble nucleation, growth and coalescence stage, and transient liquid film evaporation stage at the same heat flux. Bubble explosion can take place in the second stage. Correspondingly, five heat transfer mechanisms can be identified. For the medium boiling number range, the bubble nucleation can take place anywhere along the flow direction. Under such conditions, boiling heat transfer in microchannels is similar to the bubble nucleation, growth, and departure followed by the liquid refilling in a single cavity for the pool boiling situation. Thus, the perfect nucleate boiling heat transfer can be ensured. Higher boiling numbers cause the dominant forced convective heat transfer by the strong explosion phenomenon.

The suitable medium boiling number range causes the nucleate boiling heat transfer mechanism in MEMS evaporators, which is useful for the thermal management of IC components, to acquire a lower and uniform chip temperatures. Because the heat transfer is not dependent on the flow rate, the disturbance of the forced convective loop such as flow rate and pumping power may not affect the operation of the electronic device cooling.

Comparisons with the available boiling heat transfer correlations show that the widely accepted Chen's correlation has the correct predictive trends, even for the silicon microchannels. Most other correlations greatly overpredict the present experimental data. This may be due to the rough wall surface that is encountered for the conventional channels. New correlations are recommended.

REFERENCES

1. J.C. Chen, Correlation for Boiling Heat Transfer to Saturated Fluids in Convective Flow, *I & EC Process Design Development*, vol. 5, pp. 322–329, 1966.
2. Z.Y. Bao, D.F. Fletcher, and B.S. Haynes, Flow Boiling Heat Transfer of Freon R11 and HCFC123 in Narrow Passages, *International Journal of Heat and Mass Transfer*, vol. 43, pp. 3347–3358, 2000.
3. N.T. Nguyen, and S. Werely, *Fundamentals and Applications of Microfluidics*. Artech House, Boston, 2002.
4. Y.H. Gan, J.L. Xu, J.J. Zhou, and Y. Chen, Key Issues Related to Microscale Phase Change Heat Transfer, *Advances in Mechanics*, vol. 34, no. 3, pp. 399–407, 2004 (in Chinese).
5. G. Hetsroni, A. Mosyak, Z. Segal, and G. Ziskind, A Uniform Temperature Heat Sink for Cooling of Electronic Devices, *International Journal of Heat and Mass Transfer*, vol. 45, pp. 3275–3286, 2002.
6. G.O. Workman, J.G. Fossum, S. Krishnan, and M.M. Petella, Physical Modeling of Temperature Dependences of SOI CMOS Devices and Circuits Including Self-Heating, *IEEE Transactions on Electron Devices*, vol. 45, pp. 125–133, 1998.
7. J.L. Xu, J.J. Zhou, and Y.H. Gan, Static and Dynamic Flow Instability of a Parallel Microchannel Heat Sink at High Heat Fluxes, *Energy Conversion and Management*, vol. 46, pp. 313–334, 2005.

8. G.M. Lazarek, and S.H. Black, Evaporative Heat Transfer, Pressure Drop and Critical Heat Flux in a Small Vertical Tube with R-113, *International Journal of Heat and Mass Transfer*, vol. 25, pp. 945–960, 1982.
9. M.W. Wambsganss, D.M. France, J.A. Jendrzejczyk, and T.N. Tran, Boiling Heat Transfer in a Horizontal Small-Diameter Tube, *ASME Journal of Heat Transfer*, vol. 115, pp. 963–972, 1993.
10. T.N. Tran, M.W. Wambsganss, and D.M. France, Small Circular and Rectangular-Channel Boiling with Two Refrigerants, *International Journal of Multiphase Flow*, vol. 22, pp. 485–498, 1996.
11. P.A. Kew, and K. Cornwell, Correlations for the Prediction of Boiling Heat Transfer in Small-Diameter Channels, *Applied Thermal Engineering*, vol. 17, pp. 705–715, 1997.
12. T.S. Ravigururajan, Impact of Channel Geometry on Two-Phase Flow Heat Transfer Characteristics of Refrigerants in Microchannel Heat Exchangers, *ASME Journal of Heat Transfer*, vol. 120, pp. 485–491, 1998.
13. Y. Yan, and T. Lin, Evaporation Heat Transfer and Pressure Drop of Refrigerant R-134a in a Small Pipe, *International Journal of Heat Mass Transfer*, vol. 41, pp. 4183–4194, 1998.
14. H.J. Lee, and S.Y. Lee, Heat Transfer Correlation for Boiling Flows in Small Rectangular Horizontal Channels with Low Aspect Ratios, *International Journal of Multiphase Flow*, vol. 27, pp. 2043–2062, 2001.
15. G.R. Warrier, T. Pan, and V.K. Dhir, Heat Transfer and Pressure Drop in Narrow Rectangular Channels, *Experimental Thermal and Fluid Science*, vol. 26, pp. 53–64, 2002.
16. W. Yu, D.M. France, M.W. Wambsganss, and J.R. Hull, Two-Phase Pressure Drop, Boiling Heat Transfer, and Critical Heat Flux to Water in a Small-Diameter Horizontal Tube, *International Journal of Multiphase Flow*, vol. 28, pp. 927–941, 2002.
17. W.L. Qu, and I. Mudawar, Flow Boiling Heat Transfer in Two-Phase Micro-Channel Heat Sinks—I. Experimental Investigation and Assessment of Correlation Methods, *International Journal of Heat and Mass Transfer*, vol. 46, pp. 2755–2771, 2003.
18. J.L. Xu, S. Shen, Y.H. Gan, Y.X. Li, W. Zhang, and Q.C. Su, Transient Flow Pattern Based Microscale Boiling Heat Transfer Mechanisms, *Journal of Micromechanics and Microengineering*, vol. 15, pp. 1344–1361, 2005.
19. K.E. Gungor, and R.H.S. Winterton, A General Correlation for Flow Boiling in Tubes and Annuli, *International Journal of Heat and Mass Transfer*, vol. 29, pp. 351–358, 1986.
20. Z. Liu, and R.H.S. Winterton, A General Correlation for Saturated and Subcooled Flow Boiling in Tubes and Annuli, Based on a Nucleate Pool Boiling Equation, *International Journal of Heat and Mass Transfer*, vol. 34, pp. 2759–2766, 1991.
21. D. Steiner, and J. Taborek, Flow Boiling Heat Transfer in Vertical Tubes Correlated by an Asymptotic Model, *Heat Transfer Engineering*, vol. 13, pp. 43–69, 1992.
22. M.M. Shah, A New Correlation for Heat Transfer during Boiling Flow through Pipes, *ASHRAE Transactions*, vol. 82, pp. 66–86, 1976.
23. M.M. Shah, Chart Correlation for Saturated Boiling Heat Transfer: Equations and Further Study, *ASHRAE Transactions*, vol. 88, pp. 185–196, 1982.
24. S.G. Kandlikar, A General Correlation for Saturated Two-Phase Flow Boiling Heat Transfer Inside Horizontal and Vertical Tubes, *ASME Journal of Heat Transfer*, vol. 112, pp. 219–228, 1990.